Research Article Vol. 65, No. 6 / 20 February 2026 / Applied Optics 2001

applied optics

Computational evaluation of a measuring setup for aerosol fluorescence in integrating spheres

Julian Soltau,[1,2,*] Arne Walter,[1] Jonas Grzesiak,[1] Frank Duschek,[1] and Thomas Dekorsy[3]

[1]German Aerospace Center, Institute of Technical Physics, Langer Grund, 74239 Hardthausen, Germany
[2]AES Technology GmbH, Brauweg 40, 37073 Göttingen, Germany
[3]German Aerospace Center, Institute of Technical Physics, Pfaffenwaldring 38-40, 70569 Stuttgart, Germany
*julian.soltau@dlr.de

Received 2 October 2025; revised 1 February 2026; accepted 2 February 2026; posted 2 February 2026; published 19 February 2026

The detection of bioaerosols has become increasingly important, particularly following the COVID-19 pandemic, which highlighted the significant threat posed by airborne pathogens to human health and mobility in public transportation. However, the real-time detection of ambient aerosols remains a pressing challenge. To address this issue, we aimed to evaluate a novel measuring setup, to the best of our knowledge, for monitoring the environment through aerosol fluorescence. Fluorescence is collected by integrating spheres with dedicated detectors for selected wavelength bands to improve signal collection and, consequently, the detection limit. To determine the optimal configuration, we utilized a dedicated simulation framework to evaluate the spatial positioning of the detectors. Through the simulation, we analyzed the core aspects of such setups and their dependencies, allowing us to compare different implementation variants and propose a candidate for the experimental realization of a real-time monitor capable of classifying bioaerosols.

https://doi.org/10.1364/AO.578758

1. INTRODUCTION

Bioaerosols [1] refer to fine particles suspended within the ambient air with primarily biological components such as pollen, bacteria, viruses, or fungi. They consist of particles with sizes between 10 nm and 100 µm and can be both solid or liquid. Due to their wide range of negative health effects [2,3] and resulting relevance for public health [4], having the means to continuously judge threats by aerosols is urgently requested, in order to provide appropriate countermeasures. Especially, since people spend increasing amounts of their time in enclosed environments while they are working, at school, shopping, using (public) transportation or at home. These areas tend to show higher concentrations of bioaerosols than outdoor spaces [5–8] and lead to an increased infection risk [9]. Thus, understanding the dynamics of bioaerosols within these spaces is necessary, which leads to the necessity of reliable bioaerosol measurements. This was further highlighted by the COVID-19 pandemic, which also showed transmission through bioaerosols [10].

Although closed spaces are more of a controlled environment than outdoor areas, major gaps exist in indoor bioaerosol characterization and standardization [11]. Due to varying particle and aerosol compositions as well as a wide array of physical and biological properties, a monitoring device has to take many factors into account. Therefore, different techniques [1] are utilized to face these challenges. These are separated into online methods that are performed directly on an airflow and offline methods, which require sample collection and have a decoupled processing. This two-step process prevents a direct monitoring application, due to the delay, even though offline methods such as PCR [12,13] and DNA sequencing [14,15] are excellent for identifying the components of bioaerosols. This delay doesn't exist for online methods such as mass spectrometry [16], which measures the mass-to-charge ratio of particles to identify them. The process provides a fast and sensitive measurement, well-suited for monitoring applications, but does not work equally good for all particle sizes and is limited to ionized particles. A technique not inhibited by these factors is Raman spectroscopy. Raman spectroscopy [17,18] focuses on the vibrational frequencies of chemical bonds within molecular structures and is therefore capable of measuring a substance-specific fingerprint. This comes with the drawback of weak intrinsic Raman signals and complex data analysis and therefore is mostly applied in Raman microscopy [19]. A third method is fluorescence spectroscopy [20–22]. While it does not have the specific fingerprints of Raman spectroscopy or the simplicity of mass spectrometry, the method allows measurements on most biological components, allows for the classification of different bioaerosols and has a high intrinsic signal strength.

The classic measurement setup for fluorescence spectroscopy utilizes a laser that is perpendicular to the aerosol stream and focused on a small area of the latter. Combining a mirror and a lens, the fluorescence signal is focused toward a single detector. This is exemplarily demonstrated in [23] for single particle measurements. This arrangement is the basis for different aerosol measurement systems, with some of them being already commercially available [24]. In order to characterize the aerosol particles, these devices combine the obtained fluorescence characteristics with a measurement of the particles' elastic scattering characteristics and over different field test their capability to differentiate biological aerosols from non-biological ones has been shown [25–27]. Although this differentiation was successfully demonstrated, a classification into the respective particle classes, such as bacteria, pollen, and viruses, was not possible, due to the limitation of two/three spectral channels for the fluorescence signals. These are sufficient to identify bioaerosols, but not to classify them. Therefore, advances are made to increase the number of measured fluorescence channels [28], which, e.g., has allowed for the differentiation between different pollen taxa [29,30], but overall, a general characterization of bioaerosols has not been achieved yet.

In this paper, we perform a computational evaluation of a novel measurement setup utilizing integrating spheres for the detection of aerosol fluorescence. The integrating sphere collects the emitted signal in all solid angles, with limited losses. This allows for the usage of more spectral channels in the measurement, while maintaining the average signal in each channel. Alternatively, if no additional channels are needed, the amplified signal could enable the usage of cheaper sensors, leading to more affordable devices. While the signal collection over all solid angles dramatically increases the measured signal, many aspects, such as introduced signal losses, anisotropic effects, background noise through scattering, or geometric effects from component placement, have a nontrivial impact on the overall efficiency of the photon collection ability of such a sphere. Therefore, we simulated the photon propagation in such a setup, in order to define a setup that can be used for experimental validation.

The primary objective of this study is to evaluate the feasibility of this measurement setup and the integrating sphere's capability to enhance the photon collection efficiency for an improved spectral classification accuracy. By enabling near-omnidirectional capture of emitted fluorescence signals, the integrating sphere aims to increase the signal intensity, reduce the dependency on high-cost detectors, and support multi-channel spectral analysis. This work further seeks to identify key parameters for the experimental design and geometric configurations that minimize signal losses due to scattering, anisotropy, and background noise, thereby enabling the design of a reliable, cost-effective, and scalable fluorescence sensing system.

A comprehensive Monte Carlo simulation framework was employed to model photon propagation within the integrating sphere-based fluorescence measurement setup. The simulation accounted for key physical phenomena, including isotropic and anisotropic emission, surface reflectance properties of the sphere coating, geometric effects from component placement, and scattering-induced background noise. A synthetic dataset was generated under controlled assumptions, with defined spectral properties for aerosol and components, as well as the particle distribution within the aerosol. Key parameters such as sphere size, detector position, port sizes, and port numbers were systematically varied to evaluate their influence on overall photon collection efficiency.

2. EXPERIMENTAL BACKGROUND

To monitor ambient aerosols, the air is guided through our proposed measuring device, as shown in Fig. 1. The system is designed with an aerosol flowing through the center of the integrating sphere's inlet and outlet (along the z axis). The fluorescence-inducing laser is coupled collinearly with full overlap of the aerosol. There, the UV photons might be transmitted through the exit, scattered elastically (predominantly Mie) or absorbed and generate fluorescence. Fluorescence and elastically scattered photons either propagate into the direction of a detector where they are counted, into the direction of the aerosol inlet or outlet, or into the direction of the sphere's reflective surface. In the latter case, the photons continue their propagation process with the additional option of further interactions with the aerosol particles.

Due to the low aerosol concentrations in monitoring applications, the corresponding fluorescence signal is inherently weak and its measurement has to be optimized. As sensor positions and openings can be freely positioned at the sphere's surface, this leads to a plethora of possible configurations for such a setup. Finding a suitable configuration is a complex task, as the occurring effects combine different anisotropic elements and therefore the propagation path of the photons within the sphere cannot trivially be calculated. Toward this end, the AFIS simulation framework described in [31] is used. This framework provides the option to simulate the photons within an integrating sphere. The dominant physical effects considered within the simulation are described in Table 1. Other effects are neglected due to their low interaction probabilities. Based on the data obtained from the simulated photons, the impact of different geometries is evaluated.

3. METHODOLOGY OF THE ANALYSIS

A. Simulation Settings

For this analysis, the simulation was performed with a common set of settings, with all used distributions shown in Fig. 2. Fluorescein is used as the fluorescent base in the aerosol, as it is a fluorophore with well-known spectral behavior [32]. Absorption and emission spectra are validated with a spectrometer [33] and the measured data are used for the simulation. For the conversion from absorption to fluorescence, a wavelength-independent quantum yield of 0.92 was used, which is inline with literature for measurements with water as a solvent [32,34].

The particle size distribution is matched to normal breathing based on the measurements performed in [35]. To account for a general accumulation of particles in the air [36], a concentration of 10^3 cm^{-3} is assumed. The concentration is also assumed to be constant, corresponding to either a static aerosol within the measurement volume or a constant flow without variations in the aerosol stream. The particles are assumed to be water droplets that contain fluorescein with a concentration of 10^{-5} mol/l, to account for the small amount of fluorescent constituents

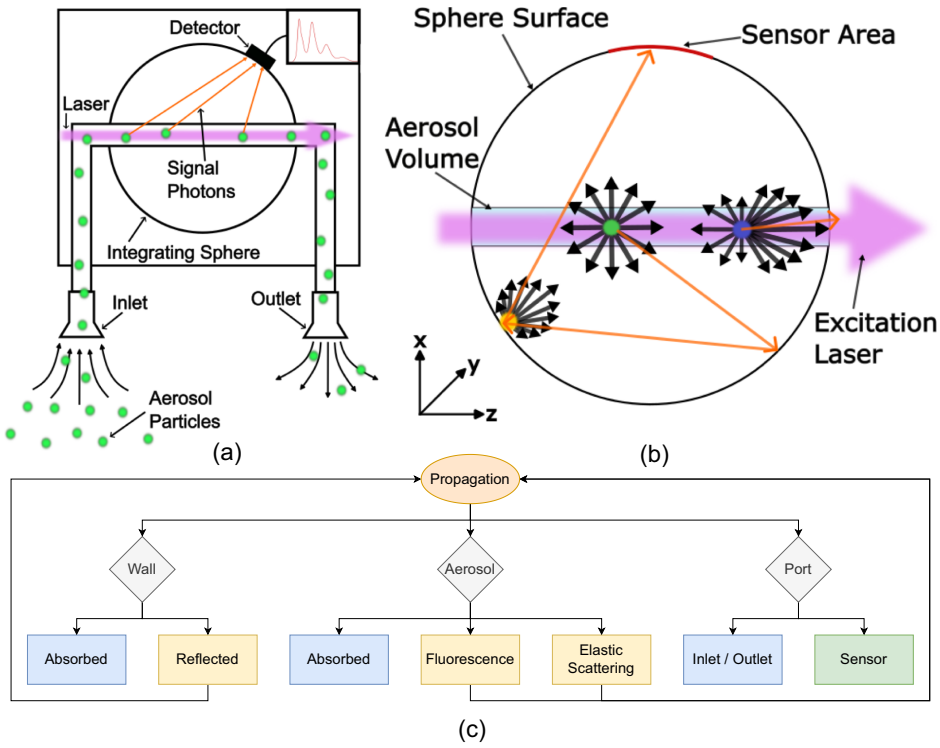

Fig. 1. Illustration of the proposed experimental setup and the prevalent physical effects involved. (a) Schematic drawing of the setup. (b) Visualization of the most important interactions inside the sphere. The directional components of fluorescence (green), Mie-scattering (blue), and diffuse reflection (yellow) are shown together with the exemplary path of two photons (orange). (c) The interaction loop for photons within the sphere based on the effects covered in Table 1.

Table 1. Physical Processes Covered within the Simulation Framework and Their Implementation

Process	Implementation
Elastic scattering	Mie-Scattering implemented Probability based on the average Mie cross-section of the medium Direction derived from the corresponding Mie-Scattering distribution
Absorption in medium	Probability based on the absorption spectrum of the medium
Fluorescence	Probability based on the aerosol properties Wavelength sampled from the emission spectrum of the medium Direction sampled from a spherical distribution
Absorption by sphere	Probability based on reflectivity of coating
Reflection by sphere	Diffuse reflection Direction sampled from cosine distribution perpendicular to the surface
Exit of sphere	Calculation of intersections between photons and openings/sensors

in bioaerosols. As fluorescein is a strong fluorophore some bioaerosols would create weaker signals, this has to be considered regarding the feasibility of a specific application. Since the simulated particles are liquid droplets, they are assumed to be spherical for all purposes within the simulation.

The integrating sphere was simulated with a PTFE coating, which is a standard coating due to its Lambertian properties [37]. Compared to other typical coatings, like gold or barium-sulfate, it achieves the highest reflectivity within the spectral regions relevant for this application. The reflectivity distribution we used is based on data supplied by a manufacturer [38] and features a reflectivity of around 99.0% over the visible range with a drop toward 98.0% for the near UV range. Additionally, a light source with a luminous power of 100 mW and a wavelength of 266 nm is assumed.

The simulation was set to calculate 10^7 photons per run, divided into bundles containing 10 photons each. This ensures the stability of the results, as the distribution of the photons over the different components has a standard deviation of less than 1‰ for these settings.

B. Parameters

The analysis is centered around the four parameters that mainly influence the spread of signal photons. For all parameters, a range of values is considered, as shown in Table 2. The value ranges are chosen based on the commercial availability of components, limitations of said components or experimental considerations, such as handling of the aerosol stream or the laser. The parameters are the following:

Sphere Diameter. This affects the length of the interaction volume as well as the number of reflections inside the sphere.
Number of Sensors. A larger number of sensors can increase the measured signal at the cost of needing more sensors and increasing the complexity of the setup.

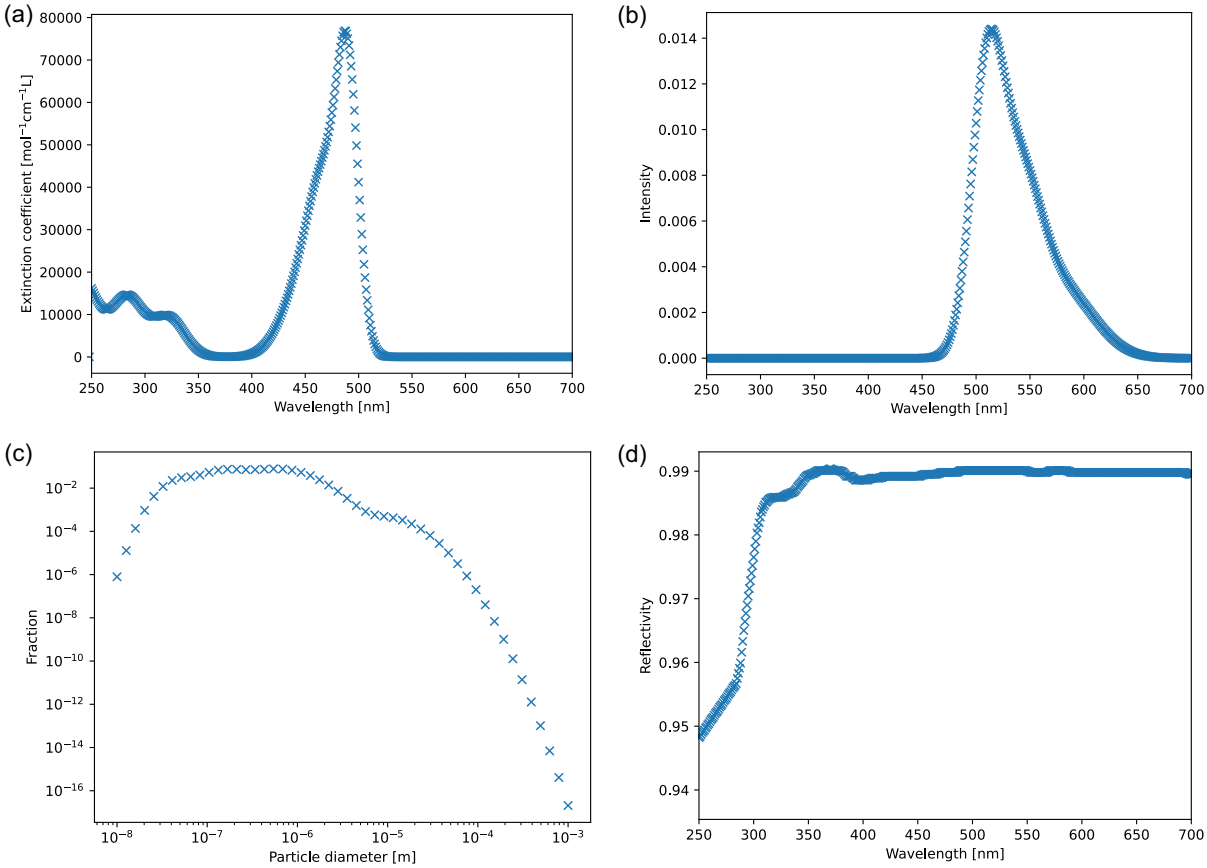

Fig. 2. Distributions used for the simulation. (a) The measured absorption spectrum of fluorescein. (b) The measured fluorescence spectrum of fluorescein. (c) The particle distribution within the aerosol (based on [35]). (d) The reflectivity of the sphere coating (based on [38]).

Table 2. Summary of the Investigated Parameter Set

Parameter	Minimum	Maximum	Step Size
Sphere diameter (cm)	4	20	2
Number of sensors	1	5	1
Sensor diameter (cm)	0.5	1.0	0.1
Aerosol port diameter (cm)	0.8	1.4	0.2

Sensor Diameter. Alternatively to using more sensors, larger sensors could be used to increase the measured signal.
Aerosol Port Diameter. The size of the ports used as the entrance and exit of the aerosol.

C. Sensor Position

In addition to the defined settings and parameters, the influence of the sensor position needs to be evaluated. For this, a setup with a fixed sphere size of 10 cm combined with a sensor and aerosol port diameter of 1 cm is used. The sensor positions are placed in 15° increments of the polar angle, as shown in Fig. 3. Due to the radial symmetry of the processes, with z being the axis of symmetry, the results at these positions can be transferred to the whole sphere. One run of the simulation is performed for each position, and the measured fraction for both fluorescence and elastically scattered photons is calculated. The measured fraction is defined as $f_m = N_m/N_T$, with the number of photons measured by a component over a simulation run N_m and the total number of simulated photons in that run N_T. The resulting values for each sensor position are also shown in Fig. 3. As seen in the plot, the detected fraction does not show much variance for the fluorescence photons. For the elastic scattering, on the other hand, an increase can be seen toward the entrance and exit, respectively, which is not large in absolute numbers, but considerable relative to the other positions.

For both cases, an increase at the aerosol entrance and exit is in line with expectations, as their relative spatial coverage for events close to them is significantly increased. For the scattered photons, this effect is stronger due to the Mie-scattering profile, which can still be recognized despite the diffuse reflection on the sphere's surface. Overall, the plot shows no significant influence of the sensor position on the measured signal. At least as long as only one sensor is involved. When multiple sensors are used, as planned in the analysis, their effect on each other has to be considered as well, since a spot with a sensor cannot reflect photons toward the sensor anymore:

$$\theta = 90° - \arccos\left(\frac{\vec{v}_p \cdot \vec{n}_s}{\|\vec{v}_p\|\|\vec{n}_s\|}\right). \quad (1)$$

To evaluate the impact multiple sensors have on to each other, the incidence angle θ of the measured photons is considered. θ is calculated according to Eq. (1) with the direction of photon

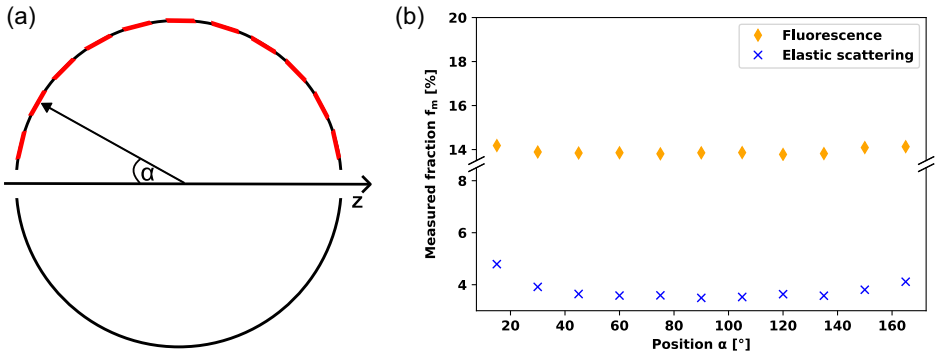

Fig. 3. Comparison of the measured photons at different positions on the sphere's surface. (a) The considered sensor positions with a step size of 15°. (b) The measured fraction at each position.

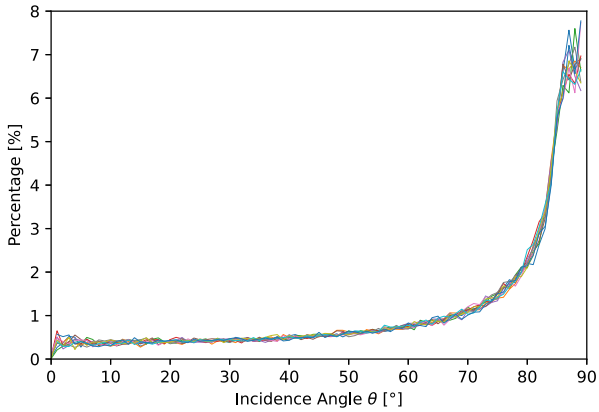

Fig. 4. Distribution of signal photons over the incidence angles for the different sensor positions. The percentages are corrected with the corresponding correction factor c_a.

bundle $\vec{v}_p$ and the outward facing surface normal of the sensor port $\vec{n}_s$. An incidence angle of 90° belongs to a photon path perpendicular to the surface, while $\theta = 0°$ equals movement parallel to the sensor plane. The distribution of incidence angles corresponds to the last point of reflection before a photon is reflected toward the sensor. As the surface area of the sphere that is covered by the different incidence angles is not equally distributed, an additional correction is applied. The correction factor c_a is calculated according to Eq. (2), with the diameter of the sphere d_S. This results in the distribution of photons reflected toward the sensor from a spot of identical size and is shown in Fig. 4 for all sensor positions:

$$c_a = (2\pi d_S \sin\theta \cos\theta)^{-1}. \quad \textbf{(2)}$$

As the plot shows, the general behavior is identical for all sensor positions. Incidence angles below 70° contribute significantly less than angles above. Therefore, sensors should not be placed in an area that corresponds to an incidence angle of more than 70° for another sensor. This is taken into consideration for the placement of sensors in our analysis.

4. RESULTS AND DISCUSSION

A. Signal and Background Levels

The first property of interest in our analysis is the available signal photons. The number of measured photons N_m ranges from 100 to 3200 per second within our examined set of parameters. These are the combined measured photons from all sensors in a run. For the individual sensors, the count rates vary between 100 and 1000 Hz. This sets the baseline for the sensitivity of possible sensors. Therefore, photon-counting level sensors are expected to be a suitable choice for the proposed measurement system, combined with a correspondingly selected geometry.

In addition to the fluorescence photons, the sensors are also exposed to background photons. Within this setup, the only notable contribution is the elastically scattered laser photons. Over the dataset, between 2.5×10^4 and 6.5×10^4 scattered photons were measured per fluorescence photon. While this would have an effect on the signal-to-noise ratio in an experiment, the small spread compared to the general order of magnitude of the ratio makes optimizing the signal level the primary focus. Moreover, filtering with at least an OD of 5 is necessary, regardless of the simulation scenario.

B. Sphere Optimization

To understand the dependencies between the different parameters, the change in the measured signal is investigated when the parameters are varied. In Fig. 5, this is shown for the sensor and aerosol port size, while the other parameters remain fixed. As seen in the heat maps, the gradient of the measured photons is significantly larger when varying the sensor size. The sensor with a diameter of 1 cm outperforms the other sensor sizes by a vast margin, regardless of the sphere size. At the same time, the maximum within each sensor size remains at a sphere size of 8 cm. The aerosol port size, on the other hand, only shows a moderate spread in the measured signal, compared to the sensor size. The maximum here is located at the smallest port size, with a diameter of 0.8 cm. But also at 1 cm port size, the values are still competitive. Similarly, the gradient over the sphere size for a fixed port size is also smaller than it is the case for the sensor size. But in contrast to the sensor size, the maximum is located at a sphere diameter of 10 cm.

To further investigate the influence of the port sizes, the data from Fig. 5 are taken again and the measured photons are plotted as a function of the port size for the different sphere sizes in Fig. 6. For each sphere size, the measured photons are normalized to their respective maximum to ensure comparability between the different sphere sizes. For the sensor port, all sphere sizes behave similarly with no significant variations between

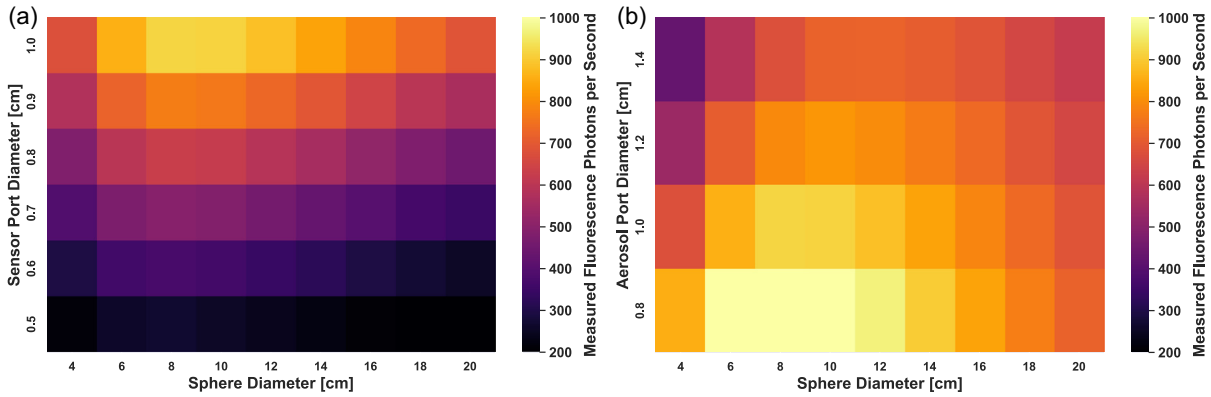

Fig. 5. Measured signal photons under varying sensor and aerosol port sizes. (a) Single sensor and 1 cm sensor diameter and (b) single sensor and 1 cm aerosol port diameter.

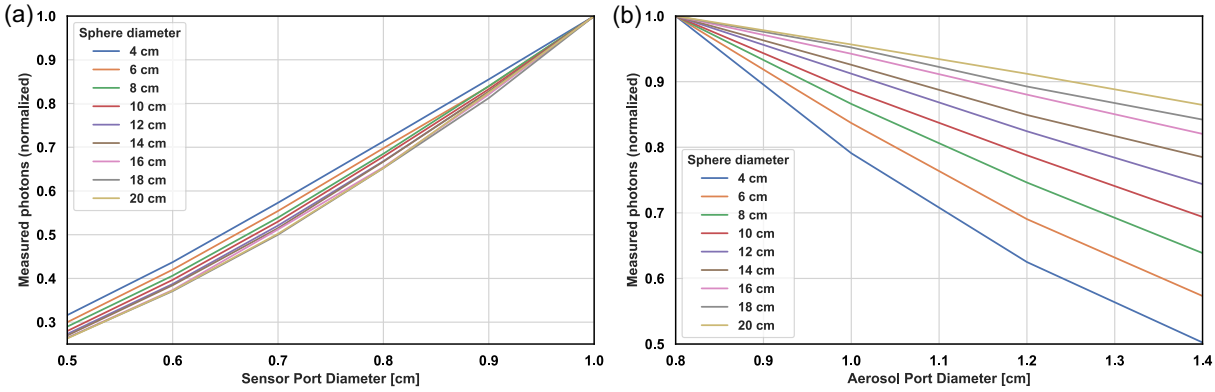

Fig. 6. Measured signal photons depending on the port sizes for different sphere diameters. The measured signal is normalized to the maximum values for each sphere size. (a) The measured signal as a function of the sensor port diameter. (b) The measured signal as a function of the aerosol port diameter.

them. For the aerosol ports, on the other hand, significant differences can be seen as small spheres have a significantly larger signal loss with increasing aerosol port diameters. But overall, the signal loss from increasing the aerosol port diameter remains lower than the signal lost by using a small sensor diameter. Therefore, the sensor diameter remains the more important parameter, while the aerosol port diameter is mostly relevant for small sphere diameters.

Figure 7 shows the behavior of the total measured photons compared to the average measured photons per sensor, for a setup with a sensor diameter of 1 cm and an aerosol port diameter of 1 cm. Within the plots, the previously mentioned different signal levels can be seen, as the average signal per sensor reaches its peak for a single sensor slightly above 900 photons per second. While the maximum of the total signal is reached by five sensors with approximately 3000 photons per second. This is also emphasized by the higher gradient in the total signal compared to the average signal per sensor. Regardless of these differences, both plots show a shift in the optimal sphere diameter depending on the number of sensors. For a single sensor, the maximum is located between 8 and 10 cm, but a setup with five sensors has its maximum at a sphere diameter of 14 cm. This means that the diameter of the sphere has to be matched to the number of sensors, when the measured signal is optimized. While we show this only with one specific configuration here, this behavior can be observed over the full parameter set this analysis is based on.

C. Possible Experimental Considerations

For an experimental realization the specific use case has to be considered first. Based on the application, the number of spectral channels and their ranges differ as they depend on the classification goal. As demonstrated by the existing measurement devices, two channels are sufficient to differentiate between biological and nonbiological aerosols, but not sufficient for a more gradual classification. On the other hand, the available signal levels from the experimental setup determine, which applications are feasible. Thus, the general impact of the sensors has to be considered first. Therefore, the achievable signal levels for different settings are compared. This is done in Table 3, which shows the highest achievable signal per sensor for different sensor diameters and numbers. As already seen in the previous section, an increase in the sensor diameter notably increases the measured photons. Therefore, its diameter should be maximized.

This also remains the case when multiple sensors are used, as the configurations with the highest average signal all use the highest sensor diameter in the parameter set. But with an increasing number of sensors, the average count rate per sensor

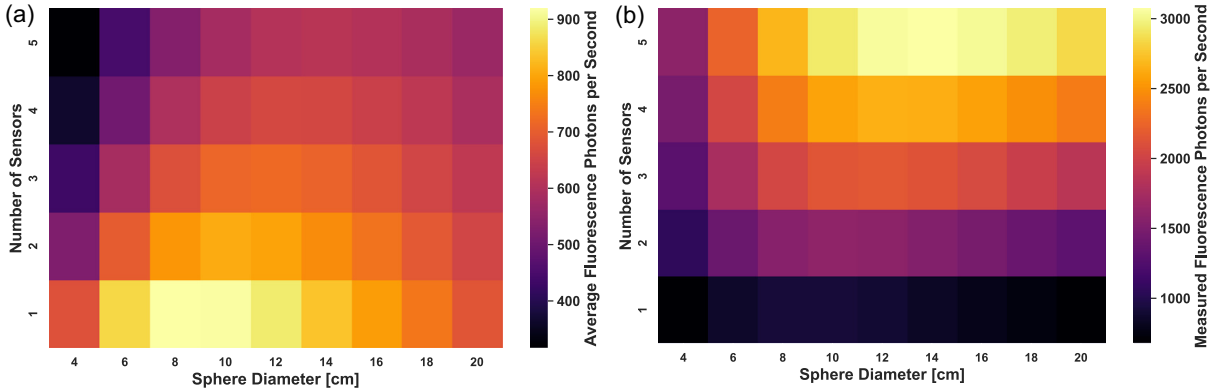

Fig. 7. Comparison of the total measured signal with the average signal per sensor for different combinations of sensors and sphere sizes, with a sensor diameter of 1 cm and an aerosol port diameter of 1 cm. (a) Average photon count rate per sensor and (b) total photon count rate.

Table 3. Highest Signal Count Rates per Sensor Achieved in the Simulation for Different Sensor Diameters and Numbers Together with the Respective Parameters[a]

Number of Sensor Ports	Sensor Diameter (cm)	Aerosol Port Diameter (cm)	Sphere Diameter (cm)	Ø Sensor Count Rate (Hz)	Total Count Rate (Hz)
1	0.5	0.8	6	323	323
1	0.6	0.8	6	447	447
1	0.7	0.8	6	583	583
1	0.8	0.8	8	732	732
1	0.9	0.8	8	896	896
1	1	0.8	8	1060	1060
2	1	0.8	10	888	1776
3	1	0.8	10	782	2346
4	1	0.8	12	707	2828
5	1	0.8	12	649	3245

[a]In the upper section, the best performing configuration for each sensor size is shown, while the lower section shows the configurations with the highest average signal for the different sensor numbers.

decreases. This is highlighted by the fact that using five sensors instead of one only leads to a three-fold increase of the total signal, while the signal in each individual channel decreases by approximately 40%. Therefore, the number of spectral channels cannot be increased arbitrarily, since the average number of photons per sensor will decrease to the point where a measurement is not feasible anymore. This is not the case within the simulated scenarios. While the average count rate decreased in the case of five sensors it still remains at a level where commercially available sensors operate and five spectral channels are already a good basis for fluorescence measurement. Therefore, such a measurement setup would generally be feasible for the measurement of aerosol fluorescence.

Additionally, if more than ten spectral channels are of interest, the usage of a spectrometer might be beneficial compared to multiple detectors. This limits the number of sensor ports, but leads to a trade-off in the diameter of the sensor port, since spectrometers are limited in their aperture size. To evaluate this, a direct comparison with the components is required, as the simulation does not account for specific component parameters such as acceptance angles and sensitivities of the sensors. Similarly, the simulation did not account for fluctuations in the aerosol properties. In the case of an experimental implementation, these have to be closely monitored to ensure the integrity of the measured data. Therefore, a thorough classification of the samples would be needed in addition to measurements of environmental conditions such as the temperature and humidity, which affect the behavior of the aerosol.

5. CONCLUSION

The simulation-based analysis of the integrating sphere-based fluorescence measurement system proposed in this work demonstrates that careful design optimization is critical for achieving high performance in ambient aerosol monitoring. The study focused on human-exhaled aerosols, representing realistic conditions for the monitoring of human-transmitted pathogenic bioaerosols. Key findings indicate that sensor selection and configuration significantly influence the system's efficiency: maximizing the sensor diameter enhances the signal collection, while using multiple sensors increases the total signal output at the expense of a reduced average signal per channel. This highlights a trade-off between spectral resolution and signal strength.

For the evaluated parameter set, a configuration combining a 12 cm diameter integrating sphere and five sensors with 1 cm diameter each emerged as optimal, balancing a sufficient number of spectral channels with the highest average signal, reaching a theoretical maximum of 600 photons per second per sensor. This is within signal levels that can be handled by photon-counting sensors, which are best suited for low-light fluorescence detection. Additionally, the analysis revealed that elastic scattering of the excitation laser's photons creates a significant background signal, necessitating spectral filters with at least five orders of magnitude suppression at the laser wavelength to ensure a sufficient signal-to-noise ratio. Given the availability of compatible sensors, integrating spheres, and filtering components, the proposed system is experimentally feasible. These results confirm the viability of the design concept and provide a clear pathway for future experimental validation and implementation in real-world aerosol fluorescence monitoring applications.

Funding. Deutsches Zentrum für Luft- und Raumfahrt.

Disclosures. The authors declare no conflicts of interest.

Data availability. Data underlying the results presented in this paper are not publicly available at this time but may be obtained from the authors upon reasonable request.

REFERENCES

1. Z. Huang, X. Yu, Q. Liu, *et al.*, "Bioaerosols in the atmosphere: a comprehensive review on detection methods, concentration and influencing factors," Sci. Total Environ. **912**, 168818 (2024).
2. J. Douwes, P. Thorne, N. Pearce, *et al.*, "Bioaerosol health effects and exposure assessment: progress and prospects," Ann. Occup. Hyg. **47**, 187–200 (2003).
3. C. Humbal, S. Gautam, and U. Trivedi, "A review on recent progress in observations, and health effects of bioaerosols," Environ. Int. **118**, 189–193 (2018).
4. G. Duffield and S. Bunn, "Indoor air quality," (2023).
5. W.-K. Jo and Y.-J. Seo, "Indoor and outdoor bioaerosol levels at recreation facilities, elementary schools, and homes," Chemosphere **61**, 1570–1579 (2005).
6. S. Faridi, M. S. Hassanvand, K. Naddafi, *et al.*, "Indoor/outdoor relationships of bioaerosol concentrations in a retirement home and a school dormitory," Environ. Sci. Pollut. Res. **22**, 8190–8200 (2014).
7. W. Yang, S. Elankumaran, and L. C. Marr, "Concentrations and size distributions of airborne influenza a viruses measured indoors at a health centre, a day-care centre and on aeroplanes," J. R. Soc. Interface **8**, 1176–1184 (2011).
8. K. K. Coleman, T. T. Nguyen, S. Yadana, *et al.*, "Bioaerosol sampling for respiratory viruses in Singapore's mass rapid transit network," Sci. Rep. **8**, 17476 (2018).
9. B. Rowe, A. Canosa, J. Drouffe, *et al.*, "Simple quantitative assessment of the outdoor versus indoor airborne transmission of viruses and COVID-19," Environ. Res. **198**, 111189 (2021).
10. R. Tellier, "COVID-19: the case for aerosol transmission," Interface Focus **12**, 20210072 (2022).
11. J. Cox, H. Mbareche, and C. Duchaine, "Field sampling of indoor bioaerosols," Aerosol Sci. Technol. **54**, 572–584 (2020).
12. H. A. Erlich, *PCR Technology: Principles and Applications for DNA Amplification* (Palgrave Macmillan UK, 1989).
13. I. M. Mackay, "Real-time PCR in virology," Nucleic Acids Res. **30**, 1292–1305 (2002).
14. J. M. Heather and B. Chain, "The sequence of sequencers: the history of sequencing DNA," Genomics **107**, 1–8 (2016).
15. V. R. Després, J. F. Nowoisky, M. Klose, *et al.*, "Characterization of primary biogenic aerosol particles in urban, rural, and high-alpine air by DNA sequence and restriction fragment analysis of ribosomal RNA genes," Biogeoscience **4**, 1127–1141 (2007).
16. L. Krásný, R. Hynek, and I. Hochel, "Identification of bacteria using mass spectrometry techniques," Int. J. Mass Spectrom. **353**, 67–79 (2013).
17. H. Jin, J. Wang, S. Jin, *et al.*, "Raman spectroscopy of potential biohazards commonly found in bio-aerosols," Spectrochim. Acta A **243**, 118753 (2020).
18. A. Sengupta, N. Brar, and E. J. Davis, "Bioaerosol detection and characterization by surface-enhanced Raman spectroscopy," J. Colloid Interface Sci. **309**, 36–43 (2007).
19. J.-X. Cheng and X. S. Xie, "Coherent anti-Stokes Raman scattering microscopy: instrumentation, theory, and applications," J. Phys. Chem. B **108**, 827–840 (2004).
20. J. Lakowicz, *Principles of Fluorescence Spectroscopy* (University of Maryland School of Medicine Baltimore, 2006), Vol. **132**.
21. L. R. Dartnell, T. A. Roberts, G. Moore, *et al.*, "Fluorescence characterization of clinically-important bacteria," PLOS ONE **8**, e75270 (2013).
22. A. Alimova, A. Katz, R. Podder, *et al.*, "Virus particles monitored by fluorescence spectroscopy: a potential detection assay for macromolecular assembly," Photochem. Photobiol. **80**, 41–46 (2004).
23. Y. L. Pan, J. Hartings, R. G. Pinnick, *et al.*, "Single-particle fluorescence spectrometer for ambient aerosols," Aerosol Sci. Technol. **37**, 628–639 (2003).
24. M. J. Fennelly, G. Sewell, M. B. Prentice, *et al.*, "Review: The use of real-time fluorescence instrumentation to monitor ambient primary biological aerosol particles (PBAP)," Atmosphere **9**, 1 (2018).
25. E. Toprak and M. Schnaiter, "Fluorescent biological aerosol particles measured with the waveband integrated bioaerosol sensor WIBS-4: laboratory tests combined with a one year field study," Atmos. Chem. Phys. **13**, 225–243 (2013).
26. Z. Chen, I. Crawford, E. Matthews, *et al.*, "Real-time field measurements of bioaerosols in the agricultural environment: concentrations, components and environmental impacts," J. Environ. Manage. **393**, 127033 (2025).
27. J.-H. Tian, C. Yan, Z. A. Nasir, *et al.*, "Real time detection and characterisation of bioaerosol emissions from wastewater treatment plants," Sci. Total Environ. **721**, 137629 (2020).
28. T. Könemann, N. Savage, T. Klimach, *et al.*, "Spectral intensity bioaerosol sensor (SIBS): an instrument for spectrally resolved fluorescence detection of single particles in real time," Atmos. Meas. Tech. **12**, 1337–1363 (2019).
29. B. Crouzy, M. Stella, T. Konzelmann, *et al.*, "All-optical automatic pollen identification: towards an operational system," Atmos. Environ. **140**, 202–212 (2016).
30. I. Šaulienė, L. Šukienė, G. Daunys, *et al.*, "Automatic pollen recognition with the Rapid-E particle counter: the first-level procedure, experience and next steps," Atmos. Meas. Tech. **12**, 3435–3452 (2019).
31. J. Soltau, A. Walter, F. Duschek, *et al.*, "AFIS - a simulation framework for detection of aerosol fluorescence with integrating spheres," Comput. Phys. Commun. **321**, 110008 (2026).
32. R. Sjöback, J. Nygren, and M. Kubista, "Absorption and fluorescence properties of fluorescein," Spectrochim. Acta A **51**, L7–L21 (1995).
33. Edinburgh Instruments, "FS5 spectrofluorometer," https://www.edinst.com/products/fs5-spectrofluorometer/ (Accessed: 09/2024).
34. D. Magde, R. Wong, and P. G. Seybold, "Fluorescence quantum yields and their relation to lifetimes of rhodamine 6G and fluorescein in nine solvents: improved absolute standards for quantum yields," Photochem. Photobiol. **75**, 327–334 (2002).
35. G. Bagheri, O. Schlenczek, L. Turco, *et al.*, "Size, concentration, and origin of human exhaled particles and their dependence on human factors with implications on infection transmission," J. Aerosol Sci. **168**, 106102 (2023).
36. B. Blocken, T. van Druenen, A. Ricci, *et al.*, "Ventilation and air cleaning to limit aerosol particle concentrations in a gym during the COVID-19 pandemic," Build. Environ. **193**, 107659 (2021).
37. B. K. Tsai, D. W. Allen, L. M. Hanssen, *et al.*, "A comparison of optical properties between high density and low density sintered PTFE," Proc. SPIE **7065**, 70650Y (2008).
38. Thorlabs, "PTFE material reflectance," https://www.thorlabs.com/images/TabImages/PTFE_Material_Reflectance-780.gif (Acccessed: 09/2024).